Hygro-elastic coupling in a 3D exact shell model for bending analysis of layered composite structures

nature communications

Article

https://doi.org/10.1038/s41467-025-59748-5

Real-time 3D temperature reconstruction in microwave cancer hyperthermia from scarce temperature measurements

Received: 10 July 2024

Accepted: 1 May 2025

Published online: 24 May 2025

Check for updates

Rossella Gaffoglio[1], Giorgio Giordanengo[1], Marco Righero[1], Marcello Zucchi[2], Maryam Firuzalizadeh[2], Giuseppe Musacchio Adorisio[1], Aurora Bellone[2], Alberto Vallan[2], Guido Perrone[2] & Giuseppe Vecchi[2]

Oncological microwave hyperthermia is a clinically proven sensitizer of radio- and chemo-therapies; it acts by selectively increasing the temperature of tumor cells by means of antenna applicators. Its current limitations mostly come from the inability to reliably predict, and hence control, temperature inside the patient during treatment, especially for deep-seated tumors. Simulations are employed in treatment planning, but due to related uncertainties invasive thermometry is necessary, usually via catheters. Being invasive, their use must be minimized and provides very limited spatial information. Here, we demonstrate an approach to obtain 3D temperature information in real time from few measurement points via massive use of high-performance simulations carried out prior to treatment. The proposed technique is tested both in a fully anthropomorphic in-silico scenario, and in an experimental controlled setting. The obtained results demonstrate the potential of the proposed method as a low-cost real-time temperature monitoring technique in cancer hyperthermia. Use with intra-luminal, minimally-invasive catheters is supported by the positive outcome experimentally obtained using data points directly acquired in the trachea-mimicking phantom structure.

Cancer is one of the major causes of death in the world, and numbers are expected to significantly increase in the coming years also due to the population ageing. In this scenario, research into techniques which allow to increase the effectiveness of current treatments and improve the quality of life (QoL) of cancer patients is of primary importance and urgency.

Thermal therapies currently play a significant role in cancer treatment, particularly when combined with other treatment methods. Depending on the temperature reached, the treatment duration, and the method of heat administration, heat therapies can be distinguished into microwave hyperthermia, ablation (RF, microwave, ultrasound), and laser therapy. While the aim of ablation is to shrink or destroy tumor cells with temperatures above 60 °C, administered for a duration usually less than 10 min[1], microwave hyperthermia (HT) consists in heating the tumor temperature to 42–44 °C for 60–90 min, which results in increased sensitivity of cancer cells to radiation and drugs. HT has been clinically demonstrated as a means for improving the treatment efficacy of radiotherapy and chemotherapy, without increasing their long-term side effects[2–6], proving particularly useful in the treatment of recurrent cancers[7–9].

The operational mechanism of hyperthermia consists in focusing the electromagnetic field generated by an antenna applicator on the tumor region, with minimal heating of the surrounding healthy tissues; for deep-seated and sub-superficial tumors, this is achieved using a

[1]Advanced Computing, Photonics & Electromagnetics, Fondazione LINKS, Torino I-10138, Italy. [2]Department of Electronics and Telecommunications, Politecnico di Torino, Torino I-10129, Italy. e-mail: giuseppe.vecchi@polito.it

phased array applicator[10,11]. Hyperthermia treatment planning (HTP) simulations are used to predict the distribution of specific absorption rate (SAR) and temperature in the treated region of interest (ROI) and find the antenna feeding coefficients which allow to selectively heat the tumor region[12–15]. This can be obtained by optimizing the SAR distribution in the ROI, using properly defined SAR-based objective functions, or, directly, the temperature; whether one approach is better than the other is still an open question in the scientific community, and both SAR-based and temperature-based optimization routines are nowadays used in the clinical practice leading to comparable results[16]. Although being the basis of HTP, simulations cannot be completely relied on for temperature monitoring, due to the high uncertainty of crucial tissue properties (such as perfusion), and even of some model equations[17–20].

Currently, the most accurate method of controlling the effective temperature in clinical practice during HT treatments employs probes encased in closed-tip catheters, which provide very limited spatial information[12,21]. A technology under development is based on measuring the temperature distribution by carrying out thermal treatments inside an MRI environment[22,23]. MR thermometry is an evolving field, but at present only provides relative temperature change data, is hampered by field heterogeneity, subject to inaccuracies in the presence of (e.g., respiratory) motion, and has difficulties measuring in fatty tissues. Widespread application of MR thermometry is also limited by the high cost of operating MRI scanners, their scarce availability, and the challenges involved in applying thermal therapies inside an MRI system. Other limitations of MR thermometry which affect more ablation than hyperthermia (due to the higher temperatures reached) are the artifacts induced by local susceptibility changes, temperature-induced variations in tissue electrical conductivity, and gas bubble formation[24,25]. Electrical impedance tomography (EIT) has also been proposed[26–29] for non-invasive and cost-effective thermometry, but it relies on sophisticated simulations that suffer from large uncertainties.

The current lack of a method that allows to provide a real-time temperature map in all points of the treated region is therefore evident, and it is a problem that concerns not only HT but all thermal therapies. The method proposed in this article consists in creating a patient-specific set of temperature simulations in the ROI, corresponding to different combinations of the constituent parameters (which are known within large uncertainty ranges), and then match this set to the scarce and limited data provided by a single closed-tip catheter to obtain a realistic 3D temperature map of the patient in real time.

Computations are often not reliable per se since a large uncertainty may affect how the parameters describing the underpinning physical system are known[20], and measurements are often scarce and affected by unavoidable noise; hence complementing information from computational science and from experimental measurements has recently gained interest in the broad topic of digital twin[30–35]. This article describes a coherent framework to seamlessly integrate these two sources of information without resorting to the full machinery of Bayesian inference that is often employed—thus avoiding the related computational burden in the online monitoring phase—and provide experimental validation of its performance in the case of temperature monitoring during a hyperthermia treatment using few temperature sensors. We used low-discrepancy sequences for picking the combinations of the constituent parameters when populating the set of patient-specific simulations. We remark that the interest here is in exploring the space of different combinations as much as possible and not in deriving any statistical measure, as it is done in instances of the Monte Carlo method[20].

Few attempts are reported in the literature aimed at enhancing the accuracy of temperature simulations while minimizing invasive thermometry. The approach proposed in this article leverages few measured samples to continuously adapt the predicted temperature distribution to better match the measured data, providing an updated estimate of the patient's temperature in real time. This differs from another method reported in the literature[18,36], where tissue parameters are estimated by fitting the simulated maps to temperature measurements and used to predict the temperature evolution without any explicit real-time check that the expected temperature matches the real one. Existing approaches that explore the possibility to find a full 3D temperature map require optimization routines to run in post-treatment, involving iterative thermal simulations and measured data[18,37]; these techniques are indeed not intended to offer a real-time feedback on the actual 3D temperature distribution, but rather to provide benefits in subsequent treatments. The proposed method, conversely, shifts the computational burden to the pre-treatment stage, creating a patient-specific library of temperature maps that can be used starting from the first application and allows to reconstruct the temperature even in the case where crucial parameters, such as perfusion, vary over time. Another line of research[38] blends a compact representation of the time evolution of the temperature in the ROI (based on a library of simulations, similarly to the method proposed here) with data from MR thermometry. At a difference from the cited approach[38], however, that compact representation does not consider the relevant issue of parameter uncertainty and MR thermometry provides more data points than temperature probes in a single closed-tip catheter, at the price of requiring a more complex equipment. As a further difference, the method proposed here may use any code to populate the simulations library, commercial or developed ad-hoc, without assuming a level of access to the inner working of the software used to build the library of temperature maps that is difficult to achieve without developing an in-house code[38].

Tests carried out both in a simulation scenario and in an experimental testbed, specifically built to simulate a hyperthermia treatment in the head and neck (H&N) region, are presented in this article to prove the feasibility of the proposed method. An estimate of the true state of the system is provided using the limited information from a single catheter, which can also be far from the tumor site and even external to the ROI, i.e. inserted in the part of the phantom that simulates the trachea, so as to mimic a non-invasive intraluminal catheter. The technique demonstrated represents an efficient way of implementing a feasible, real-time, full-3D thermometry in a minimally invasive way (if not even non-invasive in the case of intraluminal catheters). Unlike MR thermometry, the proposed approach also represents a low-cost and easy-to-deploy method, which could favor, in the future perspective, widespread use in the clinic of thermal therapies.

Results

Overview of the method and metrics

The standard HTP approach starts with the generation of a 3D segmented model of the patient, obtained from CT and MRI scans (see Fig. 1), which is then imported in a multiphysics simulation environment together with the model of the antenna applicator. Numerical solvers in HTP involve the solution of Maxwell's equations and the bioheat thermal equation, using a set of dielectric and thermal parameters (Methods). The tissue properties assigned to relevant tissues and organs of the segmented phantom are typically found in the literature, where they are reported with considerable uncertainty[17–20]. These parameters, here named $\mathbf{s}_{\text{base}}$ (Fig. 1), are indeed estimated as averages over different studies and measurements, and their values can vary significantly[18] under HT treatments, being temperature-dependent. The simulated temperature map at time t, indicated as $\mathcal{F}(\mathbf{r}, t; \mathbf{s}_{\text{base}})$, where $\mathbf{r}$ belongs to the set of mesh points in the ROI, is not reliable per se, due to the inherently uncertainty affecting the model's constituent parameters. This makes interstitial thermometry advisable during treatment[21], although it allows to control the effective temperature in a very limited number of points—this means that a hotspot that the patient does not yet perceive as pain could be present far from the temperature probes and be dangerous especially in highly thermosensitive regions (e.g., spinal cord).

https://doi.org/10.1038/s41467-025-59748-5

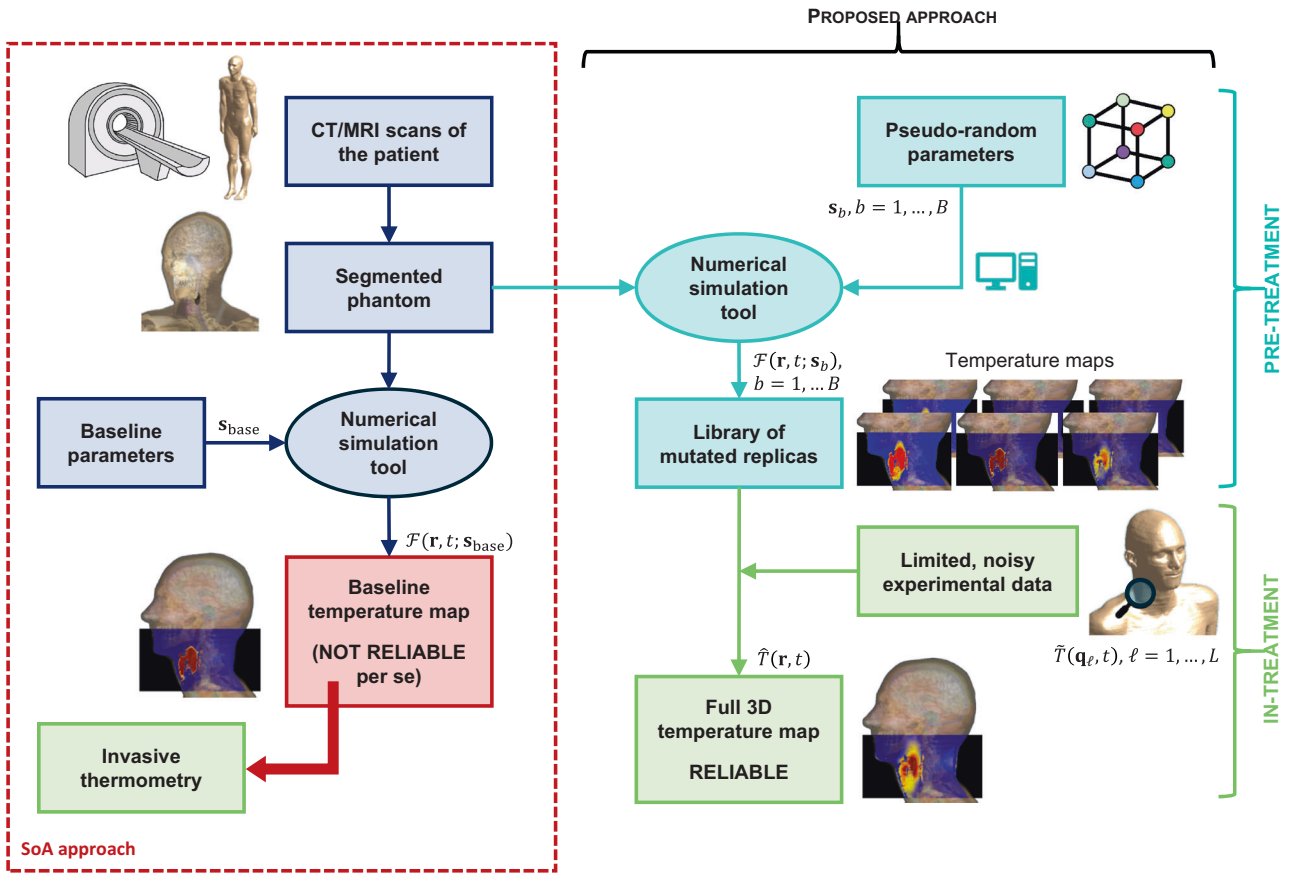

Fig. 1 | Proposed method. Flow chart reporting the approach used nowadays in the clinic to perform HT treatments (State-of-the-Art (SoA) approach) and the proposed methodology. As schematically depicted, the proposed method employs an ensemble of simulations specific to each patient, built by considering purposely mutated replicas of the patient obtained by varying the constituent parameters. Matching such ensemble of simulations prepared in the pre-treatment stage to limited and noisy data acquired during treatment guides the model towards the true state of the system and reduces the uncertainty, providing a reliable 3D temperature map of the entire region of interest in real time.

The technique proposed in this paper has the goal to use few localized temperature measurements to provide a reliable temperature map at any time and in the whole ROI. As depicted in Fig. 1, the core of the proposed procedure lies in two fundamental steps: 1) the creation in a pre-treatment stage of a library of multiphysics simulations reproducing the heating process in the ROI, obtained by purposely mutating the constituent parameters $\mathbf{s}_b$, $b = 1, \ldots, B$, within realistic variation ranges according to a low-discrepancy sequence (Sobol sequences are used); 2) the acquisition of few measurement points $\tilde{T}(\mathbf{q}_\ell, t)$, $\ell = 1, \ldots, L$, during treatment. The challenge of providing real-time maps of the temperature in the entire ROI during treatment is then addressed by selecting and combining the elements of the ensemble of multiphysics simulations in the way that best matches the scarce measurement data, leveraging the available data to reduce the uncertainty that affects simulations. The reconstruction process entails recovering the temperature map in the 3D space from a limited (noisy) set of real-time temperature measurements acquired along the direction of a fiber-optic thermometer. From a mathematical point of view, this corresponds to solve a constrained least squares problem involving the set of multiphysics simulations and the scarce available measurement points (Methods).

The feasibility of the proposed technique is here demonstrated in two different scenarios. The first scenario is a completely in-silico testbed designed following the ESHO guidelines[39], realized in the simulation software Sim4Life[40] using state-of-the-art anthropomorphic human body phantoms, where the effect of blood perfusion is included. The second scenario is an experimental mock-up reproducing a muscle-tissue equivalent phantom of the human neck heated by a phased array applicator, which has the main purpose of demonstrating the validity of the method in a system affected by real experimental errors.

To assess the accuracy of the obtained results in accordance with the current literature, we consider the median of the absolute temperature difference ΔT between the target map and the reconstructed temperature map $\hat{T}(\mathbf{r}, t)$ in the ROI, and the absolute difference of the T50 and T90 parameters[18,39], i.e., the temperature exceeded by 50% and 90% of points in the tumor region. Although these median values are measures of inaccuracy, we will refer to them as accuracies as common in the related literature[18].

The target map can be a simulated temperature map corresponding to a given combination of the constituent parameters or a set of experimental points $\tilde{T}(\mathbf{r}_m, t)$, $m = 1, \ldots, M$, distributed in the whole phantom. The reconstructed temperature map is instead obtained by applying the proposed method using the temperature information provided by the target map in few spatial points $\mathbf{q}_\ell$, $\ell = 1, \ldots, L$, located along the same direction and affected by noise (Methods).

In addition to the standard metrics, we also introduce the following goodness function $g(\chi)$:

$$g(\chi) = \frac{\text{Vol}\left(\{\mathbf{r} \in \text{ROI} : \Delta T \leq \chi\}\right)}{\text{Vol(ROI)}} \tag{1}$$

representing the relative size of the region where the absolute difference ΔT is below a certain threshold χ (°C). It should be noted that $g(\chi) = 1, \forall \chi$, denotes perfect reconstruction.

https://doi.org/10.1038/s41467-025-59748-5

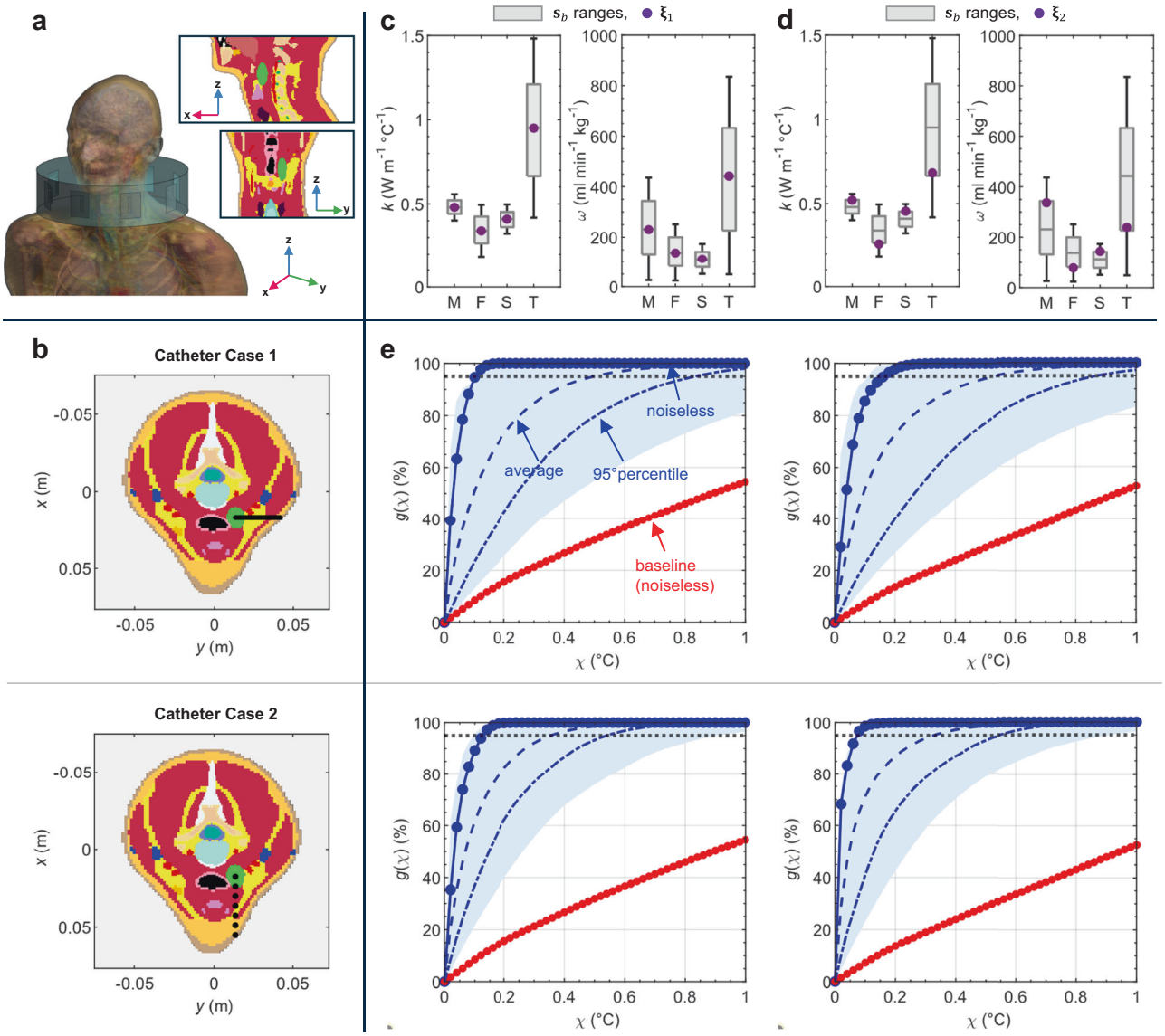

Fig. 2 | In-silico testbed results: visualization of the reconstruction error for two target maps and two different catheter configurations. a Fully anthropomorphic human phantom Duke V3.0 employed to simulate an HT treatment, using a phased array applicator made of eight patch antennas immersed in the water bolus; the inset shows the tumor target position (highlighted in green). **b** The temperature values $\widetilde{T}(\mathbf{q}_\ell, t_{ST})$ used to perform the reconstruction are acquired in the spatial points $\mathbf{q}_\ell$, $\ell = 1, \ldots, L$, (black dots) distributed along the direction of a fiber-optic thermometer inserted on the transversal (xy) plane passing through the tumor at its centroid; from top to bottom the number of points considered are: $L = 20$ (case 1) and 7 (case 2). **c**, **d** Boxplots showing the minimum, maximum, median and interval between the 25th and the 75th percentiles of the set of thermal parameters (k and ω) corresponding to key tissues in the ROI (M = muscle, F = fat + SAT, S = skin, T = tumor) when a Sobol sequence is used to sample the parameters space; superimposed dots represent the combinations of parameters $\boldsymbol{\xi}_a$ of two target maps $\mathcal{F}(\mathbf{r}, t_{ST}; \boldsymbol{\xi}_a)$, $a = 1$ (**c**), $a = 2$ (**d**). **e** Goodness function $g(\chi)$, Eq. (1): rows refer to the catheter cases (**b**), and columns represent the target maps (**c**, **d**). The blue-dot line corresponds to the reconstruction of the target map without noise; the blue-shadow region includes 2000 realizations of a Gaussian distribution function ($\mu = \pm 0.1$ °C and $\sigma = 0.2$ °C) used to introduce an error on the target map, with the blue dashed line denoting the average and the dash-dotted line indicating the 95th percentile; the red-dot line expresses the discrepancy between the target field and the baseline map (SoA simulation approach). Source data are provided as a Source Data file.

When a large set of cases is included in the study, we denote as $\mathcal{L}(\chi, \zeta)$ the likelihood that a specified fraction (ζ) of the ROI has an error below a certain threshold χ, i.e., $\mathcal{L}(\chi, \zeta) = P(g(\chi) > \zeta)$, where $g(\chi)$ is the normalized goodness function defined in Eq. (1). We finally indicate as χ_{95} the minimum χ such that $\mathcal{L}(\chi, 0.95) > 0.95$, which represents the minimum error threshold χ such that there is a 95% chance of having at least 95% of the ROI with an error lower than χ (among the number of cases considered). Lower values of χ_{95} correspond to a better reconstruction.

In-silico testbed

The in-silico testbed was implemented by using the simulation software Sim4Life V7.0.2[40], where a common hyperthermia applicator used to treat deep-seated and sub-superficial tumors in the H&N region[10,41] was reproduced and optimized to heat a target volume placed inside a realistic human phantom of the Sim4Life virtual population[42]. Figure 2a shows the realistic human phantom Duke V3.0, which is a detailed, high-resolution anatomical model of a 34-years-old male, developed from high-resolution magnetic resonance image data[42]. A tumor mass with non-uniform shape—resembling an irregular prolate spheroid—was inserted into the phantom at a realistic position in the H&N region (see Fig. 2a). The dimensions of the tumor target along the xyz axes are 16.5 mm, 13.4 mm, and 35.7 mm, while the coordinates of its centroid with respect to the considered reference system are $x_c = 18.02$ mm, $y_c = 16.15$ mm, and $z_c = 1574.9$ mm. Following the HTP workflow, the

Table 1 | In-silico testbed: baseline value and range of variation of the thermal properties considered in the reconstruction procedure

Tissue	Parameter					
	k (W m^{-1} °C^{-1})			ω (ml min^{-1} kg^{-1})		
	Baseline	Min	Max	Baseline	Min	Max
Muscle	0.49	0.40[18]	0.56	39.1[47]	19	442.8[18]
Fat (+SAT)	0.21	0.18	0.50[18]	33	20	255[18]
Skin	0.37	0.32	0.50	106	49	175
Tumor	0.51[18]	0.41[a]	1.50[18]	72.3[47]	36.15[b]	848[18]

The values without a specific reference are derived from the IT'IS database[43]. The lower bounds of thermal conductivity (k) and perfusion (ω) for the tumor have been fixed proportionally to the percentage of variation in the corresponding skin ranges, i.e., [a]80% of the baseline value; [b]50% of the baseline value.

dielectric properties were assigned to the segmented tissues according to their baseline values, i.e., the values reported in the literature[43], at the operating frequency of 434 MHz.

As illustrated in Fig. 2a, the considered HT applicator is a uniform circular array with a diameter of 256.8 mm consisting of eight patch antennas immersed in water, positioned around the neck of the phantom. The antennas are designed to work in the so-called water bolus, a doughnut-shaped bag filled with circulating demineralized water at a constant temperature in the range of 20–25 °C, used in the clinical practice to avoid overheating of the skin and favor radiation coupling into the body[44,45]. The geometrical parameters of the antennas have been optimized to resonate properly at the operating frequency. The length and the width of the optimized patch antennas are 31.0 mm and 7.2 mm, respectively, the height is 8.4 mm, while the distance of the feed to the edge is 4.96 mm.

The antenna feeding coefficients were found by applying an optimization approach commonly used in the clinical practice, aimed at maximizing the specific absorption rate (SAR) in the tumor target, minimizing the risk of overheating in the surrounding healthy regions[13] (Supplementary Notes 1, 2). The temperature map in the ROI is then obtained after assigning the thermal parameters to the different tissues, setting the thermal boundary conditions (Methods), and using the optimized SAR distribution as source term of the bioheat equation. A total input power $P_0 = 52$ W was used, which proved to be a sufficient value to reach a T50 parameter of 42.5 °C and a maximal normal tissue temperature of 43 °C[46], using the baseline thermal tissue parameters[43].

Validation of the method using the in-silico testbed

Among the dielectric and thermal parameters assigned to the different tissues of the phantom, perfusion is crucial for the calculation of the temperature profile, being characterized by the largest uncertainty[19]. In the considered testbed, we applied the proposed method to mitigate the error introduced by the uncertainty affecting thermal parameters, i.e., thermal conductivity (k) and perfusion (ω) (Methods), assigned to the most relevant tissues in the considered ROI, i.e., muscle, fat (including the subcutaneous adipose tissue, SAT), skin and the tumor mass. To build the library of multiphysics simulations the selected 8 parameters are changed by employing a Sobol sequence to explore the parameters space within the ranges of variation reported in Table 1[18,43,47], while the other properties are assigned to the tissues according to their baseline values[43]. Choosing rather wide ranges for the considered parameters (as we did in Table 1) allows the method to handle their uncertainty even under thermal stress.

Indicating with $\mathcal{F}(\mathbf{r}, t_{ST}; \boldsymbol{\xi}_a)$ a target temperature map obtained by solving the steady-state bioheat equation when a set of values $\boldsymbol{\xi}_a$ is assigned to the selected set of parameters, the proposed reconstruction method is applied assuming to know $\mathcal{F}(\mathbf{r}, t_{ST}; \boldsymbol{\xi}_a)$ only in the spatial points $\mathbf{q}_\ell$, $\ell = 1, \ldots, L$, distributed along the direction of a catheter and affected by a normally distributed noise $f_{\mathcal{N}}(\mathbf{q}_\ell; \mu, \sigma^2)$ (Methods).

Figure 2 reports the results concerning the application of the proposed method to two target maps, for two different configurations of the points used for the reconstruction and 2000 realizations of the Gaussian error ($\mu = \pm 0.1$ °C, $\sigma = 0.2$ °C). The curves displayed in Fig. 2e clearly show that the error obtained by reconstructing the target maps with the proposed method is on average lower that 0.6 °C in 95% of the ROI, in each of the reported cases (see the dashed blue lines), although the scarce points used in the reconstruction are affected by noise. Figure 2e also shows that 95% of the ROI has an error lower than 0.9 °C for 95% of the realizations. Moreover, for all the considered noise realizations (blue shaded region), the achieved error is always significantly lower than what would be obtained by simply using the baseline values (red-dot line). The accuracy of the reconstructed temperature can be quantified by the median of the difference ΔT evaluated over the noise realizations, which is always lower than 0.1 °C −while reaches about 0.9 °C when the baseline map is used. The T50 and T90 parameters can instead be predicted with a median accuracy lower than 0.4 °C and 0.3 °C, respectively, with the proposed method, and higher than 3 °C using the baseline map.

To provide a more comprehensive demonstration of the proposed method, we applied the reconstruction procedure in a vast set of cases including 8 catheters configurations (see Fig. 3a), 1860 combinations of the target and reconstruction maps, 100 noise realizations, reproduced for 3 different positions of the tumor target in the phantom Duke and in Ella cV3.1, a 26-year-old fully anthropomorphic female body phantom of the Sim4Life virtual population[42] (Fig. 3b, Methods). In each case, the reconstruction was performed using a single catheter, and a set of spatial points $\boldsymbol{q}_\ell$ spaced 2 mm and 6 mm apart. This results in 18 to 30 sensor points along each catheter in the first case, and 6 to 10 points in the second case, depending on the position considered. The χ_{95} parameter evaluated over this large set of cases is visualized in Fig. 3c: it is lower than 1.1 °C with the proposed method while can reach 4.9 °C using the baseline map. The feasibility of the proposed approach within this large set of cases can be quantified by the T50 and T90 estimators (Table 2): these parameters can be predicted with a median accuracy of 0.2 °C with the proposed method, reaching about 4 °C using the baseline map. Further increasing the spacing between the sensors to approximately 1 cm, resulting in only 4 sensors along the single catheter[48], the accuracy of the T50 and T90 parameters does not change significantly (0.3 °C, IQR 0.5 °C).

To investigate the robustness of the proposed technique when some of the patient parameters are not included in the library of multiphysics simulations, we applied our method to a set of target cases that exhibit variations in the dielectric parameters compared to the baseline values, as well as in the phantom geometry. We considered 8 catheters configurations (see Fig. 3a), 100 noise realizations, and 48 target maps including the unexpected variations (Methods), using the Duke phantom with the tumor in the position T1 (Fig. 3b). We introduced variations of 10–20% in the dielectric parameters, and geometric displacements in the range ±5 mm. The computed χ_{95} parameter (Fig. 3d) and the standard estimators (Table 2) confirm the effectiveness of the reconstruction process.

While it cannot be formally excluded the existence of two sets of parameters that correspond to two temperature distributions that are similar at the measuring positions−and thus indistinguishable−and different at all the other locations, this extensive numerical investigation shows that such problematic cases occur very rarely, if they even occur at all, as the proposed method can reconstruct the temperature distribution on a large portion of the ROI (95%) in almost all the tested cases (95%) with an error lower than 1.1 °C.

The method's capability to reconstruct temperature in real-time and manage non-linearities in key tissue parameters, such as perfusion, is demonstrated in Fig. 3e, f, where transient thermal reconstruction

https://doi.org/10.1038/s41467-025-59748-5

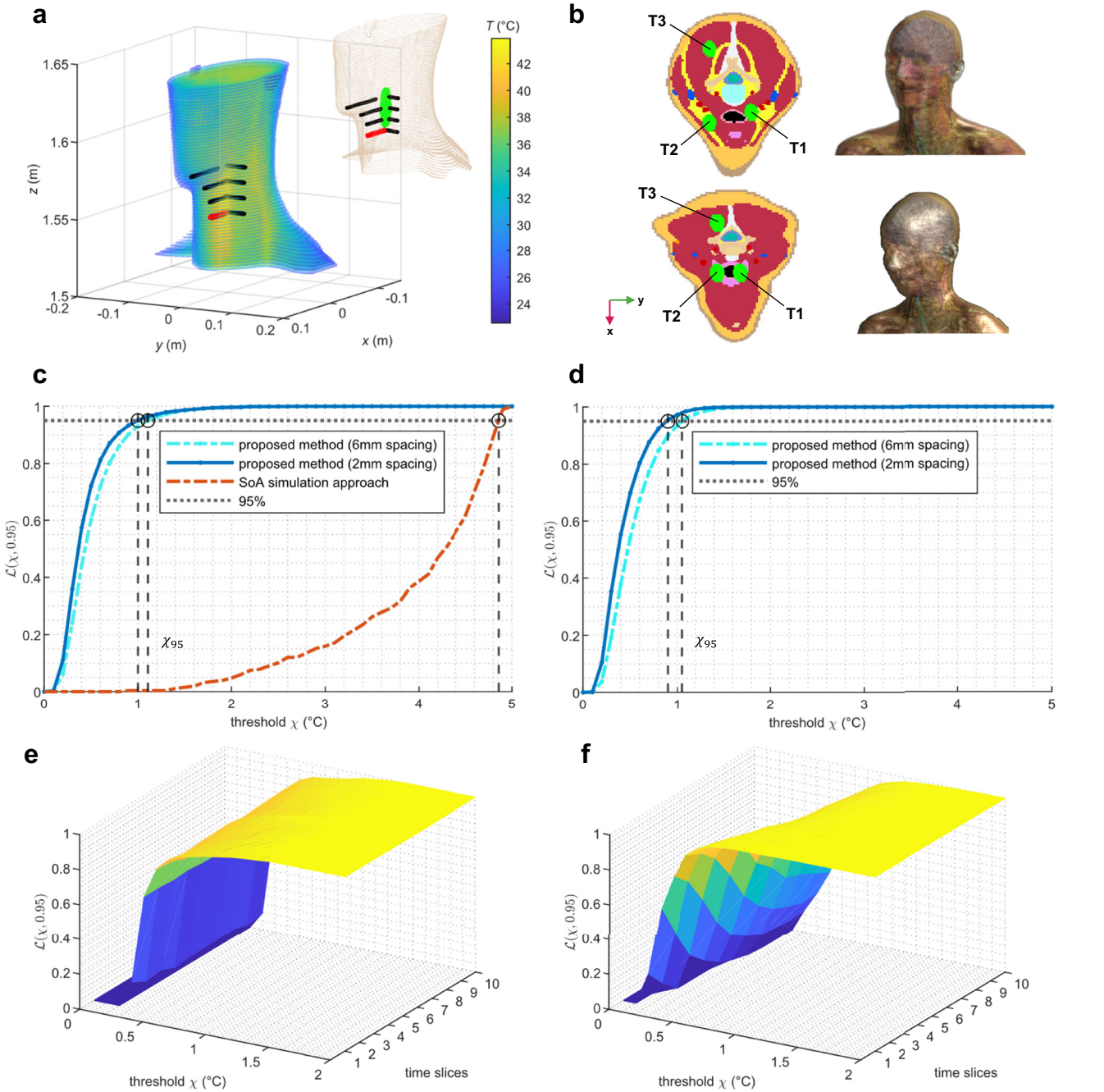

Fig. 3 | In-silico testbed results: general validity and robustness of the proposed method. a Candidate catheter positions considered for the single catheter, e.g., the red one in the picture, inserted in the ROI of the anthropomorphic phantoms and used for the reconstruction. **b** Different positions of the tumor target regions in the two phantoms Duke V3.0 (top) and Ella cV3.1 (bottom). **c**, **d** Fraction of cases considered in the study such that more than 95% of the points in the ROI have an error lower than the threshold χ. The reconstruction procedure is applied to a large number of cases, involving 1860 combinations of the target and reconstruction maps, 100 noise realizations and the two phantoms with different tumor's positions (**c**), and to a set of target cases that exhibit variations in the dielectric parameters, as well as in the phantom geometry (**d**). **e**, **f** The curves reported in (**c**, **d**) are here obtained at different times by considering transient reconstruction functions, the phantom Duke with the tumor in position T1, 100 noise realizations, 8 catheters configurations and two target maps: one obtained using optimized constant values for blood perfusion and thermal conductivity as reported in the literature[18] (**e**), the other computed using a piecewise linear temperature dependent perfusion model for muscle, fat and tumor[47] (**f**). Source data are provided as a Source Data file.

functions are used to reconstruct two target maps[47]: one with constant perfusion—as done so far—and the other incorporating a piecewise linear temperature dependent perfusion for muscle, fat and tumor. For both target maps, the reconstruction was performed in 800 cases, obtained by considering the phantom Duke with the tumor in position T1, 100 noise realizations and 8 catheters configurations with 6 mm spacing. The computed χ_{95} parameter is always lower than 1 °C for all the considered times (Fig. 3e, f), while the T50 and T90 parameters show a median accuracy in the range 0.1 ÷ 0.3 °C (IQR 0.2 °C) for both target maps.

Experimental testbed

To experimentally demonstrate the proposed technique, we developed a fully working mock-up which reproduces a hyperthermia treatment in the H&N region using a phased array applicator[10,41] and a simplified phantom mimicking the characteristics of the human neck[43]

https://doi.org/10.1038/s41467-025-59748-5

Table 2 | In-silico testbed: median and inter-quartile range (IQR) of the standard estimators using the proposed method and the SoA approach

Case study		ΔT50 (°C)			ΔT90 (°C)		
		Method (2 mm)	Method (6 mm)	SoA	Method (2 mm)	Method (6 mm)	SoA
Fig. 3c (8.9M cases)	Median	0.2	0.2	3.7	0.2	0.2	4.2
	IQR	0.4	0.4	4.7	0.4	0.4	4.5
Fig. 3d (38.4k cases)	Median	0.2	0.2	3.2	0.2	0.2	3.6
	IQR	0.2	0.3	0.5	0.3	0.3	0.5

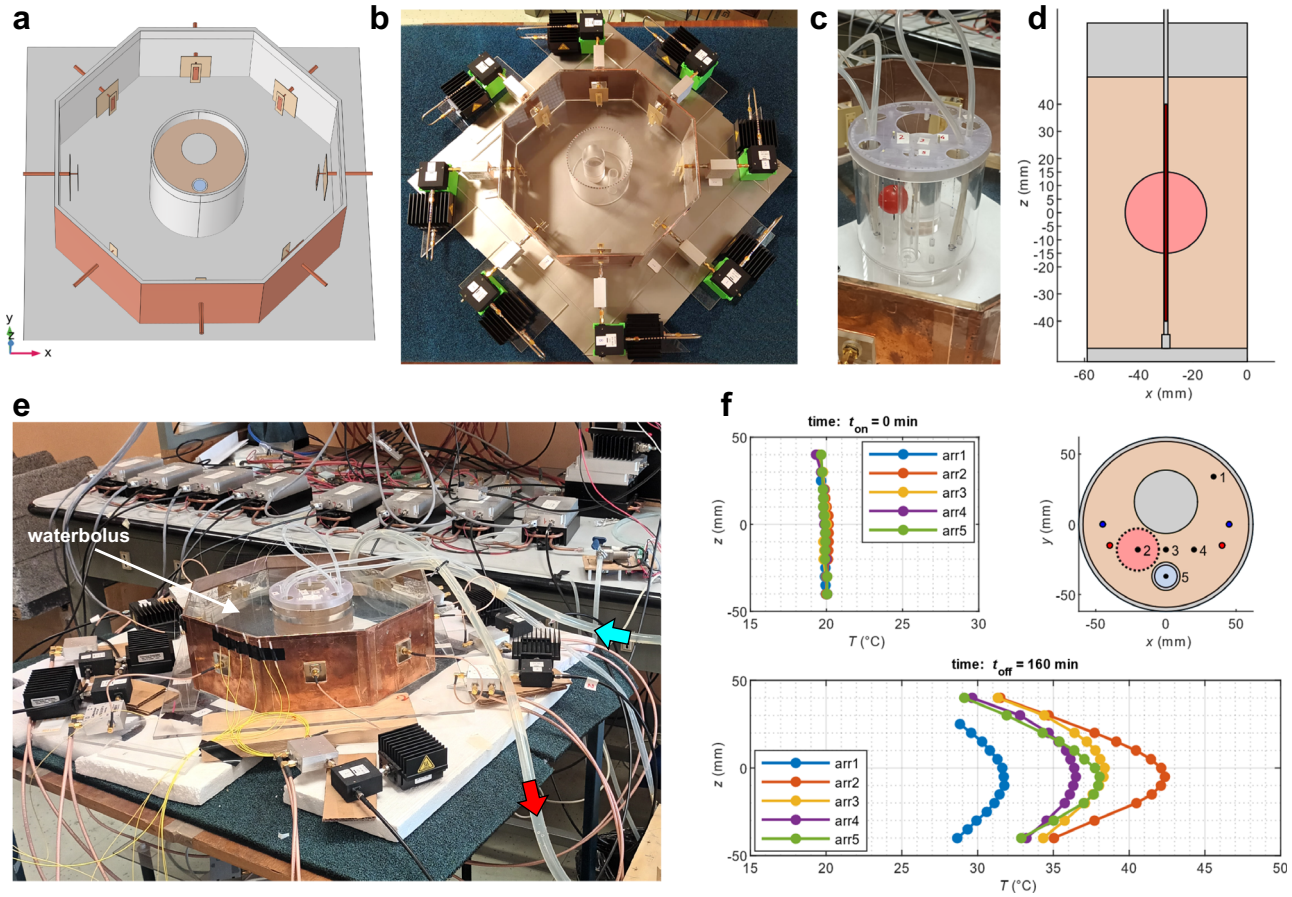

Fig. 4 | Experimental testbed: overview of the apparatus and results of the heating session. To experimentally verify the proposed method, we developed a mock-up reproducing an HT applicator for deep-seated and sub-superficial tumors in the H&N region. To measure the temperature in the realized mock-up in different locations and in real time, we used arrays of Fiber Bragg Grating (FBG) sensors, inserted along the vertical (**z**) axis. **a** In-silico model realized in COMSOL Multiphysics, reproducing the experimental prototype. **b** Experimental prototype. **c** Neck cylinder including the tumor target, the FBG arrays, and the system of pipes reproducing the cooling effect of blood vessels. **d** *z*-coordinates of the FBG sensors along the Array 2 passing through the tumor target. **e** Overview of the complete experimental apparatus. **f** Temperature read by the arrays of FBG sensors at the beginning (upper row) and at the end (lower row) of the heating session; the position of the different arrays on the *xy* plane is indicated in the upper row (right picture) and reported in Table 3, together with the *z*-coordinates of the corresponding FBG sensors. Source data are provided as a Source Data file.

(see Fig. 4). The implemented antenna applicator is a circular array of eight patch antennas with water substrate, centrally hosted on the faces of an octagonal Poly(methyl methacrylate) (PMMA) container (circumradius = 20 cm, height = 12 cm) (Fig. 4a, b). A PMMA cylinder (outer diameter = 12.4 cm, inner diameter = 11.8 cm, height = 12 cm) is placed at the center of the octagonal container and is used to house the developed phantom, created with an agar-based recipe (see Supplementary Note 3). Inside the cylinder reproducing the neck, a solid and a hollow cylinder are positioned to mimic the presence of the spine and the trachea, respectively. The outside walls of the octagonal container are covered with thin copper foils, and the space between the walls and the central phantom is filled with demineralized water to mimic the effect of the water bolus.

To reproduce the cooling effect of blood flow in the major vessels, i.e., the jugular veins and carotid arteries, a system of pipes with flowing water was inserted in the neck phantom, at specific positions (Fig. 4c). This results in a decrease of the temperature achieved in the nearby tumor mass; therefore, replicating this effect was crucial to enhance the realism of the phantom.

The simulative counterpart of the implemented prototype has been realized in the simulation software COMSOL Multiphysics[49] (Fig. 4a), used both in the design process and for temperature control. The patch antenna forming the array is the result of an optimization and refinement procedure involving both the antenna as a single element and as part of the applicator, aimed at minimizing the reflection coefficient at the operating frequency (434 MHz) (see Supplementary Note 3 for

Table 3 | Experimental testbed: coordinates of the FBG sensors along the different arrays

Array	x(mm)	y(mm)	z(mm)
1	33.94	33.94	25, 20, 15, 10, 5, 0, −5, −10, −15, −20, −25, −30, −35, −40
2	−20	−18	40, 30, 20, 15, 10, 5, 0, −5, −10, −15, −20, −30, −40
3	0	−18	40, 30, 20, 15, 10, 5, 0, −5, −10, −15, −20, −30, −40
4	20	−18	40, 30, 20, 15, 10, 5, 0, −5, −10, −15, −20, −30, −40
5	0	−37	40, 30, 20, 15, 10, 5, 0, −5, −10, −15, −20, −30, −40

The (x, y) coordinates of the arrays are displayed on the neck model in Fig. 4f. The Array 2 passes through the tumor target centroid, while the Array 5 is inserted into the hollow cylinder reproducing the trachea. The z-coordinates of the FBG sensors are indicated in Fig. 4d for the Array 2.

details). A SAR-based optimization approach was used to find the set of antenna coefficients which maximize the deposited power (SAR) in a spherical target region with radius 15 mm, centrally located in the neck phantom along the z-axis ($z_t = 0$ mm) and placed at the spatial coordinates $(x_t, y_t) = (-20, -18)$ mm (being $(0, 0)$ the coordinates of the center of the neck cylinder on the xy plane) (see Fig. 4c, d).

Implementing a proper electronic control system was necessary to apply the optimized feeding coefficients to the antennas of the array applicator and keep them constant during the heating session, with minimal losses (Methods). Figure 4e shows the experimental prototype with part of the electronic components. To mitigate the temperature increase in the water bolus due to the electromagnetic heating, the demineralized water was circulated and passed through an external water-cooling radiator by means of two pipes and a pump (see the in- and outflow directions of the pipes in Fig. 4e).

To measure the temperature in the realized mock-up in different locations and in real time, a system of Fiber Optic Sensors (FOS) has been considered. FOS interact minimally with the electromagnetic field, due to their dielectric nature; as such, they are also recommended in some guidelines for hyperthermia monitoring[46]. Among the available technologies, Fiber Bragg Gratings (FBGs) are the most widespread for their excellent combination of well-controlled fabrication process, robustness, and high sensitivity. FBGs allow for the embedding of multiple sensors within the same fiber, enabling quasi-distributed sensing with fine spatial resolution. In particular, given that the FBG arrays used for the experiments are fabricated using a femtosecond laser with the Point-by-Point (PbP) inscription method, the spatial resolution can be varied according to the requirements set by the application, being also even smaller than the physical spacing between two consecutive gratings. In the presented work, a non-uniform spacing was chosen, with higher density of the FBGs in the central section of the array where the temperature gradient is expected to be larger. The optical fibers are standard SMF-28, and the minimum spatial resolution is 5 mm. The main drawback of FBGs, as well as of all other FOS, is the intrinsic cross-sensitivity between temperature and mechanical strain; however, this issue can be effectively addressed by using a protective capillary, as employed in our setup. In the experiment, five arrays of FBG sensors[50] inserted in thin glass catheters (OD = 1.5 mm, ID = 1 mm) were placed into the neck phantom to measure the temperature along the vertical axis (see Fig. 4d). One end of the capillary is closed, while the other end was sealed with epoxy resin after the fiber was inserted. The FBG array was loosened to allow free expansion within the capillary.

The FBG sensors are interrogated using a commercial fiber grating analyzer (Luna's Hyperion Si155), setting a sampling rate of 100 Hz. To reduce noise by a factor of 10, samples are averaged over a period of 1 s. A calibration of the whole acquisition system was performed before the test, revealing an uncertainty of about 0.16 °C (coverage factor $K = 2$) for all the FBG sensors in a temperature range from 20 °C to 60 °C (see Supplementary Note 4 for details). The capillaries were positioned inside the phantom before pouring the agar-based compound thus ensuring a good contact and a small thermal resistance between the agar mixture and the sensors.

Table 4 | Experimental testbed: measured dielectric properties of the materials used in the prototype with the corresponding variation ranges

	$\varepsilon_r(-)$			σ (S m^{-1})		
	Measured	Min	Max	Measured	Min	Max
Muscle phantom	58.69	46	70	0.95	0.6	1.1
Target phantom	52.16	46	70	1.30	0.6	1.8

The measured dielectric properties were obtained with a dielectric probe (https://speag.swiss/products/dak/dak-probes/) using the phantoms prepared for the experimental heating session.

Table 3 reports the coordinates on the xy plane of the arrays numbered in Fig. 4f and the positions along the z-axis of the corresponding FBG sensors (Fig. 4d). The Array 2 was inserted in the center of the tumor target sphere, while the Array 5 was positioned in the hollow cavity of the cylinder reproducing the trachea.

Figure 4f reports the temperature measurements read by the arrays of FBG sensors at the beginning (top row) and at the end (lower row) of the heating session, where $t_{on} = 0$ min and $t_{off} = 160$ min respectively indicate the moments at which the power supply (60 W) was turned on/off. As can be observed, at the initial time, all sensors were almost at the same temperature, proving that the system was at the thermal equilibrium with an average initial temperature $T_{in} = 20$ °C. At the final time t_{off}, the temperature on the Array 2 placed in the tumor sphere is at its maximum approximately 10 °C higher than on the Array 1, which is the most distant from the target region. This confirms how the feeding coefficients obtained by maximizing the SAR in the tumor sphere led to a selective and significant heating of the target region.

Validation of the method using the experimental testbed

Following the procedure previously applied to the in-silico anthropomorphic model, the information along a single array inserted in the phantom is used to reconstruct the temperature in all the available points, using a set of purposely mutated replicas of the system; this set of reconstruction functions is generated in COMSOL Multiphysics by solving the transient version of the heat equation.

In this scenario, the simulated temperature distribution is more affected by uncertainties characterizing the dielectric properties of the phantoms used in the prototype, i.e., the muscle-mimicking phantom forming the neck and the tumor target (Table 4), and by the heat transfer coefficients introduced to describe the heat exchange between the system and the external environment. The involved parameters are changed according to a Sobol sequence to build the library of multiphysics simulations (Methods).

The goal of the proposed procedure is to use the experimental temperature values provided by the FBG sensors at the time t in a set of points $\mathbf{q}_\ell$, $\ell = 1, \ldots, L$, along one of the arrays (see Table 3) to obtain the temperature distribution in the entire phantom and then use all the experimentally available points to validate the reconstruction process.

The difference between the reconstructed map and the experimental measurements is analyzed in terms of the normalized goodness

https://doi.org/10.1038/s41467-025-59748-5

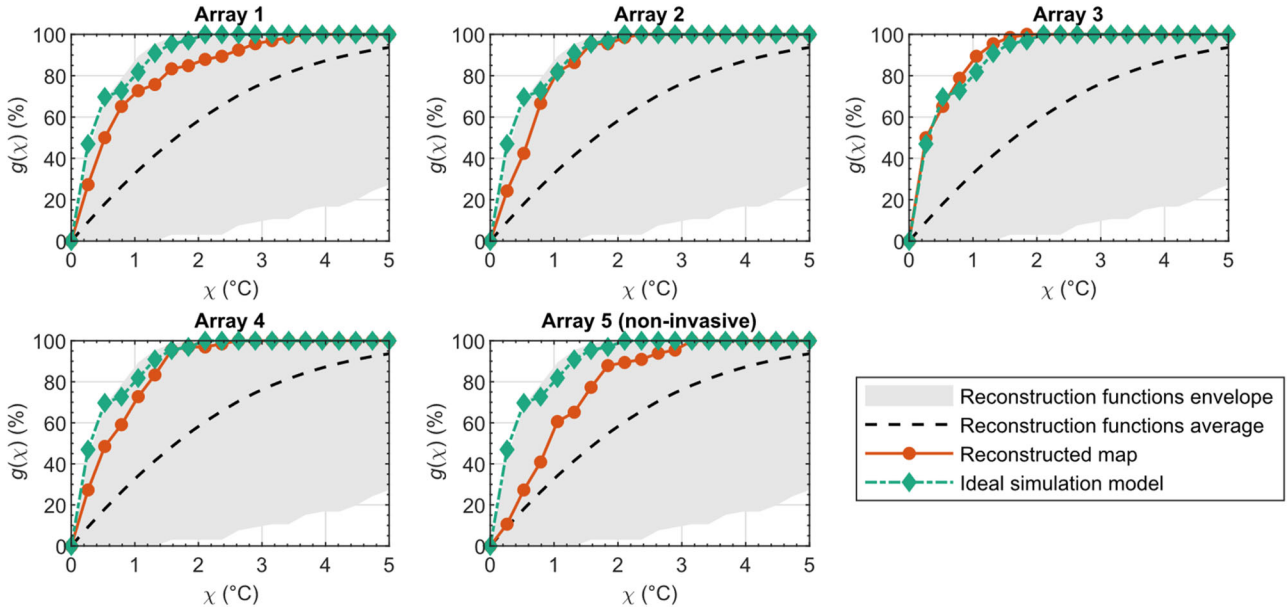

Fig. 5 | Experimental testbed results: reconstruction error indicating the fraction of points with an error below the threshold χ. The temperature map is reconstructed using the experimental data along each array (from 1 to 5, as indicated in the title of the different frames) and the normalized goodness function $g(\chi)$, Eq. (1), is evaluated in all the available points, at the end time $t = t_{off} = 160$ min (solid red-dot lines). The function $g(\chi)$ obtained by computing the error between the experiment and the ideal simulation model (dash-diamond green line) is reported for comparison, together with the envelope (gray shaded region) and the average (dashed black line) of the functions $g(\chi)$ evaluated by considering the difference between each reconstruction function and the experimental data (note that $g(\chi) = 1, \forall\chi$, denotes perfect reconstruction). Source data are provided as a Source Data file.

function $g(\chi)$ defined in Eq. (1). Figure 5 shows $g(\chi)$ evaluated when the temperature measurements along the Arrays from 1 to 5 are used individually to perform the reconstruction at the end time $t = t_{\text{off}} = 160$ min (solid red-dot curves); Fig. 5 also reports the normalized goodness function $g(\chi)$ obtained by computing the error between the experiment and the ideal simulation model (dash-diamond green line), obtained in COMSOL using the measured dielectric properties (Table 4) and the heat transfer coefficients derived by directly fitting the model to all the available data (Methods). The gray shaded region in Fig. 5 corresponds to the envelope of the functions $g(\chi)$ obtained by considering the difference between each reconstruction function and the experimental data. To estimate the effectiveness of the reconstruction (solid red-dot lines in Fig. 5) it is necessary to consider the similarity with the green curve, which provides the best possible representation of the experiment with the implemented model. As can be observed, the curves corresponding to the reconstruction (solid red-dot lines in Fig. 5) closely approximate the curve of the ideal model for almost all the arrays used for the reconstruction, and the error remains lower than what would occur on average by not applying the proposed method (dashed black line in Fig. 5).

The accuracy of the predicted temperature is here estimated using the absolute difference (ΔT) between measured and reconstructed temperature values over all the available probes and during the complete heating session (we considered 17 time samples). Table 5 shows the median and the IQR of ΔT evaluated when each array is individually considered to perform the reconstruction. As can be observed, the error achieved is included in the range 0.4÷0.6 °C, resulting reasonably higher for the array farthest from the target region (Array 1) and for the one inserted in the trachea (Array 5).

Table 5 | Experimental testbed: temperature reconstruction accuracy over all probes and the complete heating session duration

	ΔT (°C)				
	Array 1	Array 2	Array 3	Array 4	Array 5
Median	0.5	0.4	0.4	0.4	0.6
IQR	0.9	0.6	0.5	0.6	0.9

Discussion

One of the major drawbacks to widespread application of microwave hyperthermia in cancer therapy is the lack of a temperature monitoring system able to reliably trace (and even predict) the temperature in the whole ROI throughout the entire duration of the treatment (60–90 min). Invasive thermal probes provide accurate thermometry (about 0.2 °C accuracy[51]), but the information is strictly limited to a scarce number of locations[12], and their use must be reduced to the bare minimum to avoid severe treatment-related morbidities[52]. Simulations, while able to provide the needed spatial information, are not reliable: the main hurdle is the large uncertainty characterizing thermal tissue properties, which vary among patients and under thermal stress[18]. Other solutions to the temperature monitoring problem are still at the research stage and often involve expensive and complex equipment, as an MRI scanner[23,53].

In this work, we have proposed a method which allows to obtain a real-time 3D temperature map in the patient's region of interest from few, noisy, measurement points, which can also be intraluminal (non-invasive), thus circumventing the issues of the other techniques. The reliable reconstructed temperature map is intended to be used by a treatment-supervising physician, or as feedback for automatic real-time-adaptive treatment approaches[13,54], to increase the efficacy and safety of the procedure. The presented method has been verified in a specific context, which is that of microwave hyperthermia, but the applicability of the proposed technique extends to heat therapies in general, where the ability to monitor temperature accurately becomes increasingly crucial as the involved temperatures rise, along with the associated risk of irreversible tissue damage (e.g., in ablation treatments[25,55]). Moreover, we focused our demonstration on the H&N region, a challenging site due to tissue heterogeneity and the presence of thermosensitive regions like the spinal cord; however, the presented technique could be generally applied to all other regions where thermal therapies are used[4,39].

To demonstrate the validity of the proposed method, we have considered two different scenarios reproducing an HT treatment in the H&N region. In the first scenario, we tested our procedure using fully anthropomorphic phantoms; here, we reconstructed the temperature map corresponding to a combination of thermal parameters of the major tissues involved (target map) starting from few noisy points along a fixed direction. To perform an exhaustive analysis, the method was applied to about two thousand target maps in a wide range of cases (Fig. 3a–c). The T50 and T90 treatment quality parameters exhibit a median accuracy of 0.2 °C (IQR 0.4 °C) over the large set of cases considered (Table 2), strongly outperforming the performance achieved with simulations based on literature values (SoA), i.e., 4 °C median accuracy. The achieved accuracies align with the estimates considered promising in the relevant literature[18], suggesting that the proposed method is a good candidate for accurate 3D temperature dosimetry in HTP. The method proved to be robust against unexpected variations in parameters not included in the reconstruction process, as well as against geometric displacements (Fig. 3d). The T50 and T90 parameters can be predicted with a median accuracy of 0.2 °C, even introducing variations of 10–20% in the dielectric parameters, and displacements of the phantom in the range ±5 mm (Table 2).

In the second scenario, the possibility to apply the proposed technique in a non-invasive way, i.e., using RF-compatible intraluminal thermometry, has been addressed; here, the procedure was experimentally tested using a mock-up reproducing an HT treatment in the neck region. Temperature monitoring was performed using arrays of FBGs sensors. The median temperature accuracy reached when each array is individually considered as known when performing the reconstruction for all probes (along all the arrays) and for the complete treatment duration is in the range 0.4÷0.6 °C (Table 5), demonstrating acceptable values even when the array used for the reconstruction is inserted into the phantom's structure mimicking the trachea. Being obtained in a real environment, these values represent an upper bound to the accuracies estimated in this article, which could likely be further enhanced by increasing control over the implemented setup.

In the proposed technique, mutated replicas of the simulated system are used for the creation of a framework where these replicas coexist and interact with scarce measurements, to provide an estimate of the true state with reduced uncertainty. In this perspective, the proposed method could be applied in principle also when the measured data is only indirectly related to the physical quantities of interest, by modeling the target system along with the measurement process. This would allow the proposed method to be used not only with fiber-optic temperature probes, but also with a set of scarce and indirect measurements provided by non-invasive methods such as the electrical impedance tomography[26–29].

Possible limitations of the proposed technique are related to the level of accuracy of the model used to describe the physics of the system, which is the Pennes bioheat equation[56] in the presented work. The method could be applied in principle to more complex models[57,58], where high-performance computing techniques will likely be required to handle the higher computational burden. Further studies are also planned to test the robustness of the proposed method in the presence of spatial inhomogeneities of crucial tissue parameters such as perfusion.

The validation of the method using phantoms presented in this article provides the necessary initial testing of the proposed technique. The proposed method proves to be an effective solution to address the problem of temperature monitoring: it strongly outperforms SoA simulations based on literature values; it provides comparable accuracies as the optimization methods currently proposed in the literature[18] but in real-time; it does not present the issues of MR thermometry; it is low-cost and has shown to be effective with non-invasive measurements.

In light of the achieved results, we believe that this work and future tests with clinical data could contribute to the development of an effective means to plan and control HT treatments, enhancing the application of HT in cancer therapies.

Methods

Proposed methodology

To describe the mathematical formulation of the proposed method, let us indicate with $T(\mathbf{r},t)$ the temperature distribution at the spatial point $\mathbf{r}$ and time t. Given L temperature values $\widetilde{T}(\mathbf{q}_\ell,t)$, acquired in the spatial points $\mathbf{q}_\ell$, $\ell=1,\ldots,L$, and inherently affected by measurement uncertainties, we want to approximate the temperature distribution $\hat{T}(\mathbf{r},t)$ in the whole ROI as a finite superposition of B reconstruction functions ϕ_b, i.e.:

$$\hat{T}(\mathbf{r},t)=\sum_{b=1}^{B} w_b(t)\,\phi_b(\mathbf{r},t), \tag{2}$$

where $w_b(t)$ are the corresponding weights. The reconstruction functions $\phi_b(\mathbf{r},t)$ used in Eq. (2) are temperature distributions obtained with multiphysics simulations performed according to the clinical practice by reproducing the hyperthermia applicator and the patient's ROI in a simulation environment[59], where a set of constituent parameters is assigned to the model. Indicating with the N-tuple $\mathbf{s}_b$ a set of values assigned to N relevant parameters used in the simulation solver, the reconstruction function ϕ_b in Eq. (2) can be expressed with the notation $\mathcal{F}(\mathbf{r},t;\mathbf{s}_b)$, where $\mathbf{r}$ belongs to the set of mesh points in the simulated ROI.

The main goal of the proposed method is the possibility to obtain a real-time 3D reconstruction of the temperature distribution in the patient's region of interest (ROI) treated with a hyperthermia applicator, using few spatially-limited (noisy) measurement points acquired along the direction of a fiber-optic thermometer.

To mitigate the ill-posed nature of this inverse problem, regularization techniques are employed. The weights w_b in Eq. (2) are determined by minimizing the discrepancy between the data points $\widetilde{T}(\mathbf{q}_\ell,t)$, $\ell=1,\ldots,L$, and the approximation given by Eq. (2) evaluated at the same spatial positions and at the same time, namely $\hat{T}(\mathbf{q}_\ell,t)$. Among the different regularization techniques tested[60–62], the most robust method was found to be the linear least squares problem, given by:

$$\min_{\mathbf{w}\in\mathbb{R}^B}\sum_{\ell=1}^{L}\left(\sum_{b=1}^{B} w_b(t)\mathcal{F}(\mathbf{q}_\ell,t;\mathbf{s}_b)-\widetilde{T}(\mathbf{q}_\ell,t)\right)^2 \tag{3}$$

with the following additional constraints:

$$\sum_{b=1}^{B} w_b=1 \text{ and } w_b\geq 0\ \forall b=1,\ldots,B. \tag{4}$$

The constrained least squares (CLS) method expressed by Eqs. (3) and (4) is the approach used in all the examples reported in this article to obtain the reconstructed 3D temperature map, Eq. (2), from a set of few noisy temperature values. This CLS problem is solved using the Matlab routine lsqlin, that recasts the problem as a quadratic one with linear constraints and uses an interior-point method to solve it[63,64].

In-silico testbed

The temperature values $\mathcal{F}(\mathbf{q}_\ell,t_{ST};\mathbf{s}_b)$, $b=1,\ldots,B$, in Eq. (3) are evaluated by solving the steady-state version of the bioheat equation in the ROI for B combinations $\mathbf{s}_b$ of the selected set of parameters, while $\mathbf{q}_\ell$, $\ell=1,\ldots,L$, indicate the points along a specific direction in the ROI, mimicking the acquisition points of a fiber-optic thermometer. In the examples reported in this article, two thermal parameters have been varied for four tissues in the ROI, for a total of $N=8$ parameters, while B has been fixed to 70, that is a value for which by adding further reconstruction functions the reconstructed map no longer varies

significantly. Using a desktop computer with i7-7700 processor and 64 GB RAM, the computation of this set of maps took less than 5 h, considering 3.771 MCells in the ROI.

The L temperature values used for the reconstruction are obtained from target maps $\mathcal{F}(\mathbf{r}, t_{ST}; \boldsymbol{\xi}_a)$, where $\boldsymbol{\xi}_a$, $a \in \{1, \ldots, A\}$, are combinations of the selected constituent parameters, corresponding to sequence elements different from the sets $\mathbf{s}_b$, $b \in \{1, \ldots, B\}$. The reconstruction of a target map using the pre-computed set of reconstruction functions takes approximately 0.05 s. To assess the robustness of the proposed method in the presence of noisy data, a Gaussian noise is added to the temperature values used for the reconstruction, which can be written in the form:

$$\widetilde{T}(\mathbf{q}_\ell, t_{ST}) = \mathcal{F}(\mathbf{q}_\ell, t_{ST}; \boldsymbol{\xi}_a) + f_{\mathcal{N}}(\mathbf{q}_\ell; \mu, \sigma^2) \tag{5}$$

where $f_{\mathcal{N}}$ is a function generating an array of random errors, normally distributed with mean μ and variance σ^2. The target maps considered in Fig. 2 correspond to two examples of Sobol's extraction of the parameters $\boldsymbol{\xi}_a$; in the first case ($\boldsymbol{\xi}_1$) the parameters are all in the middle of the corresponding variation ranges (see Fig. 2c), in the second case ($\boldsymbol{\xi}_2$) the parameters alternate between the first and the third quartile (see Fig. 2d).

In the more general study reported in Fig. 3c, the reconstruction procedure was implemented by performing 10 permutations of 256 elements of a Sobol sequence, such that 70 maps served as reconstruction functions, while the remaining maps were treated as target maps. This was repeated for 3 tumor positions, two phantoms, 100 noise realizations and 8 catheters configurations (Fig. 3a, b) arranged along the x- and y-axes starting from $z_c - 20$ mm to $z_c + 10$ mm, being z_c the z-coordinate of the tumor centroid. In the analysis reported in Fig. 3d, we considered 40 target maps obtained by varying the effective conductivity and the real relative permittivity of muscle, fat (+SAT), skin and tumor according to a Sobol sequence within ±20% and ±10% of their baseline values[20], respectively, and 8 target maps corresponding to a displacement of the phantom of $(-5, -2, +2, +5)$ mm along the vertical z-axis (Supplementary Note 2). For the transient study we considered 140 reconstruction functions with constant perfusion values, evaluated at 10 times evenly spaced in the period from 6 to 36 min after the power-on, 1 tumor position (T1) in the phantom Duke, 100 noise realizations and 8 catheters configurations (Fig. 3a), for two different target maps: one with constant perfusion values and thermal conductivity as optimized in the literature[18] (Fig. 3e), the other with piecewise temperature dependent perfusion values for the muscle, fat and tumor tissues[47,65] (Fig. 3f). Each transient thermal simulation required a computational time of approximately 30 min.

Experimental testbed

Concerning the application of the proposed method to the experimental testbed, the reconstruction functions in Eq. (2) are temperature maps $\mathcal{F}(\mathbf{r}, t; \mathbf{s}_b)$, $b \in \{1, \ldots, B\}$, provided by COMSOL Multiphysics using combinations of parameters $\mathbf{s}_b$ including both the dielectric properties of the phantoms (Table 4) and the heat transfer coefficients used to model the heat exchange with the surrounding environment.

To mitigate errors in the positioning of the array system along the z-axis, the reconstruction functions $\mathcal{F}_k(\mathbf{r} + \Delta z_k \hat{\mathbf{z}}, t; \mathbf{s}_b)$, where $\Delta\mathbf{z}$ is a vector of shifts, are included in Eq. (2). In the described application of the proposed method, we considered $B = 200$ Sobol sequence variations $\mathbf{s}_b$, $b \in \{1, \ldots, B\}$, and a vector of shifts $\Delta\mathbf{z} = (-5, -2, 0, 2, 5)$ mm, which resulted in having 1000 reconstruction functions. Using the L acquisition points along one of the arrays to retrieve the weights with the CLS method (Eqs. (3) and (4)), the other temperature values provided by the FBG sensors are used as benchmarks to establish the accuracy of the reconstruction.

Modeling equations and parameters

In HTP simulations, a set of constituent parameters needs to be assigned to the different tissues forming the patient's segmented phantom within the ROI to solve Maxwell's equations and the bioheat thermal equation. This applies to any situation where the heating of human tissues due to electromagnetic radiation needs to be studied. Concerning the electromagnetic analysis, the essential parameters include the effective conductivity σ (S m^{-1}) and the real relative permittivity ε_r (dimensionless). These parameters play a critical role in governing the behavior of electromagnetic fields within the tissues and are essential for accurately predicting the specific absorption rate (SAR) distribution during HT simulations, defined as:

$$\mathrm{SAR} = \frac{\sigma}{2\rho}|\mathbf{E}|^2, \tag{6}$$

where ρ (kg m^{-3}) is the tissue density and $\mathbf{E}$ (V m^{-1}) represents the electric field generated by the HT applicator, obtained by solving Maxwell's equations in the ROI. Subsequently, the simulated SAR acts as the external heating source in thermal simulations where the Pennes' bioheat equation (PBHE)[56] or variations of this method[57,58] are employed to model the interaction between external heat sources and human body tissues. In this article, we considered the time-dependent Pennes' bioheat equation, whose expression is given by:

$$\rho C_p \frac{\partial T}{\partial t} = \nabla \cdot (k \nabla T) + \rho \mathrm{SAR} - \rho_b C_{p,b} \omega \rho (T - T_a), \tag{7}$$

where T (°C) is the temperature, C_p (J kg^{-1} °C^{-1}) is the tissue specific heat, k (W m^{-1} °C^{-1}) is the tissue thermal conductivity, $\rho_b = 1060$ kg m^{-3} and $C_{p,b} = 3890$ J kg^{-1} °C^{-1} are the volume density and the specific heat of blood, respectively, T_a (°C) is the arterial blood temperature, and ω (ml min^{-1} kg^{-1}) is the tissue-specific volumetric blood perfusion rate. In Eq. (7), the metabolic heat generation term is not reported, being negligible with respect to the external heat source. Throughout the article, when we mention steady-state bioheat equation, we imply a vanishing time-dependent term ($\partial T/\partial t$) in Eq. (7). Conversely, if we refer to not having bioheat contribution, we mean that the last term in Eq. (7) (i.e., $\rho_b C_{p,b} \omega \rho (T - T_a)$) is neglected, and we simply indicate Eq. (7) as heat equation.

Feeding coefficients optimization

A fundamental step in HTP consists in finding the optimal excitation coefficients of the signals feeding a microwave phased array applicator, which is typically used for the treatment of sub-superficial and deep-seated tumors. The goal is to apply proper optimization techniques to find the antenna coefficients that maximize the temperature increase (to 42–44 °C) in the target region, minimizing the risk of hotspots in healthy tissues. An approach to do this consists in finding the set of antenna coefficients that maximize the specific absorption rate (SAR) in the tumor target, using properly defined SAR-based objective functions[13,14,66]; this optimization method exploits the well assessed correlation between SAR, temperature increase, and clinical outcome[67], and only involves the electromagnetic fields, allowing to formulate the optimization as a convex optimization problem with respect to the unknown excitations[66]. Although computationally fast, this method optimizes the temperature increase indirectly, and the final temperature profile could be altered by the effect of thermal boundary conditions[68]. Another approach used in the clinical practice to find the antenna coefficients aims at directly optimizing the temperature in the tumor region, using temperature-based objective functions[12,15]. While directly addressing the quantity of interest, i.e. the temperature distribution, this second method has a higher computational cost, solving the bioheat equation at each step of the

optimization procedure, and is affected by the large uncertainty characterizing thermal tissue parameters, such as perfusion[19].

In the present work, a SAR-based optimization approach[13] has been applied in both the considered scenarios (i.e., in-silico and experimental testbeds) to find the optimal excitation coefficients of the array that maximize the deposited power in the tumor region while minimizing the risk of hotspots in the surrounding healthy tissues (Supplementary Note 1).

Thermal boundary conditions

The thermal model needs to be completed by an initial condition ($T = T_{in}$ at $t = t_{on}$, being t_{on} the initial time) and proper boundary conditions (B.C.), which describe the thermal interaction of the system with the surrounding environment. In the simulation scenarios described in this article, the following convective heat flux boundary condition was applied:

$$\hat{\mathbf{n}} \cdot (k\nabla T) = h(T_{ext} - T), \tag{8}$$

where $\hat{\mathbf{n}}$ is the unit vector normal to the considered boundary, h (W m^{-2}°C^{-1}) is the heat transfer coefficient, and T_{ext} (°C) is the external reference temperature.

In the in-silico testbed, generated in the simulation software Sim4Life[40], boundary conditions have been set according to the current literature[18]. A convective heat flux B.C. (Eq. (8)) was applied at the interface between the neck and the water bolus, with $h = 82$ W m^{-2}°C^{-1} and $T_{ext} = 20$ °C, and on the internal boundary of the trachea, with $h = 50$ W m^{-2}°C^{-1} and $T_{ext} = 30$ °C[69]. Moreover, the initial temperature T_{in} in the tissues was set to 37 °C.

Regarding the in-silico model implemented in COMSOL Multiphysics to provide the simulated temperature distribution in the experimental testbed, thermal boundary conditions were set to reproduce the experimental scenario as faithfully as possible. The initial temperature in the simulated phantom was fixed according to the average temperature $T_{in} = 20$ °C read by the FBG sensors at the beginning of the heating session (see Fig. 4f, time $t = t_{on}$). The boundary condition in Eq. (8) was applied at the following interfaces: phantom upper boundary–air (h_{tn}), phantom lower boundary–air (h_{bn}), phantom lateral walls–water bolus (h_{wb}). A heat flux boundary condition was introduced at the interface between the bottom of the phantom and the air since during the heating session the prototype was lifted from the workbench with proper supports to avoid thermal insulation. The temperatures (T_{ext} in Eq. (8)) of the surrounding air and the water bolus were set to 21 °C and 19.8 °C, respectively, as measured during the heating session. An additional heat flux B.C. was added at the boundaries of the silicon pipes reproducing the main vessels, with $h = 10$ W m^{-2}°C^{-1} and a controlled external temperature of 25.6 °C.

The presence of PMMA walls of non-negligible thickness around the neck phantom makes it difficult to estimate the heat transfer coefficients. Due to the high degree of uncertainty, all the heat transfer coefficients were included in the proposed reconstruction procedure and allowed to vary within wide ranges (10÷80 W m^{-2}°C^{-1}) for the creation of the set of mutated replicas of the system. The heat transfer coefficients used in the ideal simulation model are: $h_{tn} = 30$ W m^{-2}°C^{-1}, $h_{bn} = 20$ W m^{-2}°C^{-1}, and $h_{wb} = 55$ W m^{-2}°C^{-1}, derived by minimizing the discrepancy between all the measured temperatures and the corresponding simulated values.

Electronic setup

The first element of the electronic chain is a signal generator (HP-Agilent/Keysight 8648A) operating at 434 MHz, whose output is connected to a 1:8 power splitter to feed the antennas of the array. The phase and the amplitude delivered to each antenna are voltage-controlled by means of a phase shifter (PS) and a variable gain amplifier (VGA), respectively. A closed-loop electronic control system was implemented to correctly set the PS and VGA control voltages via a microcontroller unit (MCU) and a 16-bit DAC board. The final stage of the feeding chain consists in a Power Amplifier (PA) that boosts the signal coming from each PS to the desired power level. During the entire heating session the phases and the amplitudes provided to the antennas were locked to the desired values by the electronic control algorithm, with a maximum error lower than 1° for the phase and equal to ±0.03 dBm for the amplitude. This proves the efficacy of the implemented closed-loop control algorithm and also the prototype's ability to maintain a constant feeding to the antennas.

Temperature acquisition system

The Fiber Optic Sensors (FOS) used in this work are arrays of Fiber Bragg Grating (FBG) sensors. Other fiber sensor technologies rather than FBG, such as those based on fluorescence or Fabry-Perot cavities, are less suitable for embedding in a single fiber. Indeed, while quasi-distributed sensing is still possible with these technologies, the sensor designs would be bulkier and the interrogation systems more complex. Distributed sensing methods, such as those exploiting Rayleigh or Brillouin scattering, have also been investigated[70], but these approaches tend to be slower, less accurate, and more expensive than FBG-based sensing.

The commercial interrogator employed in the experimental testbed (Luna's Hyperion Si155) has four independent inputs, allowing for the acquisition of up to four FBG arrays. To increase the number of monitored points, the setup also incorporates a four-port optical switch connected to one of the interrogator channels. After averaging, the temperature sampling rate—and thus the temporal resolution—becomes 1 sample per second for the channels directly connected to the analyzer (arrays 1,2,3 in Fig. 4f), and 1 sample every 6 s for the multiplexed channels (arrays 4,5 in Fig. 4f). The full measurement chain composed by the FBG arrays, the patch cords, the interrogator, the optical switch and the acquisition and processing software was calibrated just before the test using a temperature sensor calibrator (Fluke 9142 field Dry-Well), a calibrated platinum sensor and a specifically manufactured calibration aluminum insert with 2 mm × 120 mm holes.

Experimental testbed: dielectric parameters variation ranges

The phantoms used in the experimental prototype are the muscle tissue-mimicking phantom filling the neck cylinder and the tumor target sphere (see Fig. 4c). The tumor sphere was created with a different agar-based recipe with respect to the surrounding muscle phantom, in which the electrical conductivity was increased in order to stress the differences in the material properties of the two compounds. This was performed to capture the heterogeneity of human tissues while using only two different types of phantoms.

The simulated temperature distribution obtained in the simulation solver COMSOL Multiphysics can be affected by uncertainties characterizing both the dielectric and thermal parameters of the materials used in the prototype. Since the effect of blood perfusion is not reproduced, and the thermal conductivity of the agar compound is rather stable and do not differ for the two phantoms, only the uncertainties in the dielectric properties were included in the reconstruction procedure.

Table 4 reports the considered variation ranges for the dielectric properties of the muscle and target phantoms. The real relative permittivity of the two phantoms and the effective conductivity of the muscle phantom were supposed to vary within ±20% and ±25%, respectively, of the corresponding baseline values for the human muscle tissue at 434 MHz[43] ($\varepsilon_r = 56.9$, $\sigma = 0.805$ S m^{-1}). The upper bound of the effective conductivity for the target phantom was increased by approximately 60% of the maximum value for the muscle phantom, to reflect the significant addition of salt in the recipe used for the preparation of the target. The measured values reported in Table 4

were instead obtained from measurements carried out directly on the phantoms prepared for the heating session using a commercial dielectric probe.

Reporting summary

Further information on research design is available in the Nature Portfolio Reporting Summary linked to this article.

Data availability

All data generated in this study have been deposited in the Code Ocean database (https://doi.org/10.24433/CO.3617548.v1). Source data are provided with this paper.

Code availability

All codes used in the analyses performed in this article are available on Code Ocean (https://doi.org/10.24433/CO.3617548.v1).

References

1. Lubner, M. G., Brace, C. L., Hinshaw, J. L. & Lee, F. T. Jr. Microwave tumor ablation: mechanism of action, clinical results and devices. *J. Vasc. Interv. Radiol.* **21**, S192–S203 (2010).
2. Franckena, M. et al. Long-term improvement in treatment outcome after radiotherapy and hyperthermia in locoregionally advanced cervix cancer: an update of the Dutch Deep Hyperthermia Trial. *Int. J. Radiat. Oncol. Biol. Phys.* **70**, 1176–1182 (2008).
3. Cihoric, N. et al. Hyperthermia-related clinical trials on cancer treatment within the clinicaltrials.gov registry. *Int. J. Hyperthermia* **31**, 609–614 (2015).
4. Datta, N. R. et al. Local hyperthermia combined with radiotherapy and-/or chemotherapy: recent advances and promises for the future. *Cancer Treat. Rev.* **41**, 742–753 (2015).
5. Datta, N. R., Rogers, S., Gómez Ordóñez, S., Puric, E. & Bodis, S. Hyperthermia and radiotherapy in the management of head and neck cancers: a systematic review and meta-analysis. *Int. J. Hyperthermia* **32**, 31–40 (2016).
6. Kroesen, M. et al. Confirmation of thermal dose as a predictor of local control in cervical carcinoma patients treated with state-of-the-art radiation therapy and hyperthermia. *Radiother. Oncol.* **140**, 150–158 (2019).
7. Vernon, C. C. et al. Radiotherapy with or without hyperthermia in the treatment of superficial localized breast cancer: results from five randomized controlled trials. International Collaborative Hyperthermia Group. *Int. J. Radiat. Oncol. Biol. Phys.* **35**, 731–744 (1996).
8. Bakker, A. et al. Temperature and thermal dose during radiotherapy and hyperthermia for recurrent breast cancer are related to clinical outcome and thermal toxicity: a systematic review. *Int. J. Hyperthermia* **36**, 1024–1039 (2019).
9. Overgaard, J. et al. Randomised trial of hyperthermia as adjuvant to radiotherapy for recurrent or metastatic malignant melanoma. *Lancet* **345**, 540–543 (1995).
10. Paulides, M. M. et al. The HYPERcollar: a novel applicator for hyperthermia in the head and neck. *Int. J. Hyperthermia* **23**, 567–576 (2007).
11. Crezee, J. et al. Improving locoregional hyperthermia delivery using the 3-D controlled AMC-8 phased array hyperthermia system: a preclinical study. *Int. J. Hyperthermia* **25**, 581–592 (2009).
12. Kok, H. P. et al. Current state of the art of regional hyperthermia treatment planning: a review. *Radiat. Oncol.* **10**, 196 (2015).
13. Rijnen, Z. et al. Clinical integration of software tool VEDO for adaptive and quantitative application of phased array hyperthermia in the head and neck. *Int. J. Hyperthermia* **29**, 181–193 (2013).
14. Bellizzi, G. G. et al. The potential of constrained SAR focusing for hyperthermia treatment planning: analysis for the head & neck region. *Phys. Med. Biol.* **64**, 015013 (2018).
15. Kok, H. P. et al. High-resolution temperature-based optimization for hyperthermia treatment planning. *Phys. Med. Biol.* **50**, 3127–3141 (2005).
16. Kok, H. P. et al. Predictive value of simulated SAR and temperature for changes in measured temperature after phase-amplitude steering during locoregional hyperthermia treatments. *Int. J. Hyperthermia* **35**, 330–339 (2018).
17. Balidemaj, E. et al. Hyperthermia treatment planning for cervical cancer patients based on electrical conductivity tissue properties acquired in vivo with EPT at 3T MRI. *Int. J. Hyperthermia* **32**, 558–568 (2016).
18. Verhaart, R. F. et al. Accurate 3D temperature dosimetry during hyperthermia therapy by combining invasive measurements and patient-specific simulations. *Int. J. Hyperthermia* **31**, 686–692 (2015).
19. De Greef, M., Kok, H. P., Correia, D., Bel, A. & Crezee, J. Optimization in hyperthermia treatment planning: the impact of tissue perfusion uncertainty. *Med. Phys.* **37**, 4540–4550 (2010).
20. Groen, J. A., Crezee, J., van Laarhoven, H. W. M., Bijlsma, M. F. & Kok, H. P. Quantification of tissue property and perfusion uncertainties in hyperthermia treatment planning: multianalysis using polynomial chaos expansion. *Comput. Methods Programs Biomed* **240**, 107675 (2023).
21. Kok, H. P. & Crezee, J. Hyperthermia treatment planning: clinical application and ongoing developments. *IEEE J. Electromagn. RF Microw. Med. Biol.* **5**, 214–222 (2021).
22. Van Rhoon, G. C. & Wust, P. Introduction: non-invasive thermometry for thermotherapy. *Int. J. Hyperthermia* **21**, 489–495 (2005).
23. Adibzadeh, F. et al. Systematic review of pre-clinical and clinical devices for magnetic resonance guided radiofrequency hyperthermia. *Int. J. Hyperthermia* **37**, 15–27 (2020).
24. Zhu, M., Sun, Z. & Ng, C. K. Image-guided thermal ablation with MR-based thermometry. *Quant. Imaging Med. Surg.* **7**, 356–368 (2017).
25. *Risk of tissue overheating due to inaccurate magnetic resonance thermometry - Letter to Health Care Providers* (U.S. Food and Drug Administration, 2021).
26. Conway, J., Hawley, M. S., Seager, A. D., Brown, B. H. & Barber, D. C. Applied potential tomography (APT) for non-invasive thermal imaging during hyperthermia treatment. *Electron. Lett.* **21**, 836–838 (1985).
27. Moskowitz, M. J., Ryan, T. P., Paulsen, K. D. & Mitchell, S. E. Clinical implementation of electrical impedance tomography with hyperthermia. *Int. J. Hyperthermia* **11**, 141–149 (1995).
28. Paulsen, K. D., Moskowitz, M. J., Ryan, T. P., Mitchell, S. E. & Hoopes, P. J. Initial in vivo experience with EIT as a thermal estimator during hyperthermia. *Int. J. Hyperthermia* **12**, 573–591 (1996).
29. Poni, R. et al. Feasibility of temperature control by electrical impedance tomography in hyperthermia. *Cancers* **13**, 3297 (2021).
30. Chaudhuri, A. et al. Predictive digital twin for optimizing patient-specific radiotherapy regimens under uncertainty in high-grade gliomas. *Front. Artif. Intell.* **6**, 1222612 (2023).
31. Kapteyn, M. G., Pretorius, J. V. R. & Willcox, K. E. A probabilistic graphical model foundation for enabling predictive digital twins at scale. *Nat. Comput. Sci.* **1**, 337–347 (2021).
32. Hernandez-Boussard, T. et al. Digital twins for predictive oncology will be a paradigm shift for precision cancer care. *Nat. Med.* **27**, 2065–2066 (2021).
33. Laubenbacher, R., Mehrad, B., Shmulevich, I. & Trayanova, N. Digital twins in medicine. *Nat. Comput. Sci.* **4**, 184–191 (2024).
34. Willcox, K. & Segundo, B. The role of computational science in digital twins. *Nat. Comput. Sci.* **4**, 147–149 (2024).
35. Foundational Research Gaps and Future Directions for Digital Twins. *National Academies of Sciences, Engineering, and Medicine* (The National Academies Press, 2024).

36. Verhaart, R. F. et al. Temperature simulations in hyperthermia treatment planning of the head and neck region: rigorous optimization of tissue properties. *Strahlenther Onkol.* **190**, 1117–1124 (2014).
37. Raaymakers, B. W. et al. Determination and validation of the actual 3D temperature distribution during interstitial hyperthermia of prostate carcinoma. *Phys. Med. Biol.* **46**, 3115–3131 (2001).
38. VilasBoas-Ribeiro, I. et al. POD–Kalman filtering for improving noninvasive 3D temperature monitoring in MR-guided hyperthermia. *Med. Phys.* **49**, 4955–4970 (2022).
39. Paulides, M. M. et al. ESHO benchmarks for computational modeling and optimization in hyperthermia therapy. *Int. J. Hyperthermia* **38**, 1425–1442 (2021).
40. Sim4Life, version 7.0.2. https://zmt.swiss/sim4life/ (2022).
41. Paulides, M. M., Bakker, J. F., Zwamborn, A. P. M. & Van Rhoon, G. C. A head and neck hyperthermia applicator: theoretical antenna array design. *Int. J. Hyperthermia* **23**, 59–67 (2007).
42. Gosselin, M. C. et al. Development of a new generation of high-resolution anatomical models for medical device evaluation: the Virtual Population 3.0. *Phys. Med. Biol.* **59**, 5287–5303 (2014).
43. Hasgall, P. A. et al. IT'IS database for thermal and electromagnetic parameters of biological tissues. Available: http://www.itis.ethz.ch/database (2018).
44. Van der Gaag, M. L., De Bruijne, M., Samaras, T., van der Zee, J. & van Rhoon, G. C. Development of a guideline for the water bolus temperature in superficial hyperthermia. *Int. J. Hyperthermia* **22**, 637–656 (2006).
45. Rijnen, Z. et al. Quality and comfort in head and neck hyperthermia: a redesign according to clinical experience and simulation studies. *Int. J. Hyperthermia* **31**, 823–830 (2015).
46. Trefná, H. D. et al. Quality assurance guidelines for superficial hyperthermia clinical trials: I. Clinical requirements. *Int. J. Hyperthermia* **33**, 471–482 (2017).
47. Drizdal, T., Paulides, M. M., van Holthe, N. & van Rhoon, G. C. Hyperthermia treatment planning guided applicator selection for sub-superficial head and neck tumors heating. *Int. J. Hyperthermia* **34**, 704–713 (2018).
48. Paulides, M. M. et al. The clinical feasibility of deep hyperthermia treatment in the head and neck: new challenges for positioning and temperature measurement. *Phys. Med. Biol.* **55**, 2465–2480 (2010).
49. COMSOL Multiphysics, version 6.1. www.comsol.it (2023).
50. Bellone, A. et al. Preliminary analysis of the estimation of tissue thermal parameters for tumor laser ablation with minimally invasive techniques. In: *Proceedings of the IEEE International Conference on Instrumentation and Measurement* (IEEE, 2024).
51. Carrapiço-Seabra, C. et al. Application of the ESHO-QA guidelines for determining the performance of the LCA superficial hyperthermia heating system. *Int. J. Hyperthermia* **40**, 2272578 (2023).
52. Van der Zee, J., Peer-Valstar, J. N., Rietveld, P. J., de Graaf-Strukowska, L. & van Rhoon, G. C. Practical limitations of interstitial thermometry during deep hyperthermia. *Int. J. Radiat. Oncol. Biol. Phys.* **40**, 1205–1212 (1998).
53. Paulides, M. M., Dobsicek Trefna, H., Curto, S. & Rodrigues, D. B. Recent technological advancements in radiofrequency and microwave-mediated hyperthermia for enhancing drug delivery. *Adv. Drug Deliv. Rev.* **163**, 3–18 (2020).
54. Kok, H. P. et al. Online adaptive hyperthermia treatment planning during locoregional heating to suppress treatment-limiting hot spots. *Int. J. Radiat. Oncol. Biol. Phys.* **99**, 1039–1047 (2017).
55. Geoghegan, R., ter Haar, G., Nightingale, K., Marks, L. & Natarajan, S. Methods of monitoring thermal ablation of soft tissue tumors – a comprehensive review. *Med. Phys.* **49**, 769–791 (2022).
56. Pennes, H. H. Analysis of tissues and arterial blood temperatures in the resting human forearm. *J. Appl. Physiol.* **1**, 93–122 (1948).
57. Arkin, H., Xu, L. X. & Holmes, K. R. Recent developments in modeling heat transfer in blood perfused tissues. *IEEE Trans. Biom. Eng.* **41**, 97–107 (1994).
58. Kotte, A. et al. A description of discrete vessel segments in thermal modelling of tissues. *Phys. Med. Biol.* **41**, 865–884 (1996).
59. Paulides, M. M. et al. Simulation techniques in hyperthermia treatment planning. *Int. J. Hyperthermia* **29**, 346–357 (2013).
60. Hastie, T. Ridge regularization: an essential concept in data science. *Technometrics* **62**, 426–433 (2020).
61. Candès, E., Romberg, J. & Tao, T. Stable signal recovery from incomplete and inaccurate measurements. *Commun. Pure Appl. Math.* **59**, 1207–1223 (2006).
62. Candès, E. & Tao, T. The Dantzig selector: statistical estimation when p is much larger than n. *Ann. Statist.* **35**, 2313–2351 (2007).
63. Altman, A. & Gondzio, J. Regularized symmetric indefinite systems in interior point methods for linear and quadratic optimization. *Optim. Methods Softw.* **11**, 275–302 (1999).
64. Vanderbei, R. J. & Carpenter, T. J. Symmetric indefinite systems for interior point methods. *Math. Program.* **58**, 1–32 (1993).
65. Lang, J., Erdmann, B. & Seebass, M. Impact of nonlinear heat transfer on temperature control in regional hyperthermia. *IEEE Trans. Biomed. Eng.* **46**, 1129–1138 (1999).
66. Iero, D. A. M., Crocco, L. & Isernia, T. Thermal and microwave constrained focusing for patient-specific breast cancer hyperthermia: a robustness assessment. *IEEE Trans. Antennas Propag* **62**, 814–821 (2014).
67. Lee, H. K. et al. Superficial hyperthermia and irradiation for recurrent breast carcinoma of the chest wall: prognostic factors in 196 tumors. *Int. J. Radiat. Oncol. Biol. Phys.* **40**, 365–375 (1998).
68. Gaffoglio, R., Righero, M., Giordanengo, G., Zucchi, M. & Vecchi, G. Fast optimization of temperature focusing in hyperthermia treatment of sub-superficial tumors. *IEEE J. Electromagn. RF Microw. Med. Biol.* **5**, 286–293 (2021).
69. McFadden, E. R. Jr. et al. Thermal mapping of the airways in humans. *J. Appl. Physiol.* **58**, 564–570 (1985).
70. Beccaria, A. et al. Temperature monitoring of tumor hyperthermal treatments with optical fibers: comparison of distributed and quasidistributed techniques. *Opt. Fiber Technol.* **60**, 102340 (2020).

Acknowledgements

This work was supported by the project RESOLVED-K – Real-Time Temperature Maps Reconstruction in Microwave Cancer Hyperthermia, Project identification code: 121322 - (2024.0238), awarded to G.V. A special thank goes to the colleagues of the departments DISAT and DENERG, Politecnico di Torino, for the thermal characterization of the phantom, and to Giuseppe Franco, from Fondazione LINKS, for the help provided in the implementation of the antenna applicator.

Author contributions

G.V. proposed, conceptualized and supervised the whole study. R.G., M.F. and M.R. worked on the in-silico testbed and the analysis of the results. G.G., R.G., M.Z. and G.M.A. designed the experimental testbed and carried out the experimental sessions. A.B., A.V. and G.P. performed the measurements with the system of fiber optic sensors and analyzed the temperature results. R.G. performed the study concerning the application of the proposed method to the experimental testbed and analyzed the results. M.F. and M.R. wrote the part of the article concerning the in-silico testbed, while R.G. wrote the experimental part. All authors discussed the results and reviewed the manuscript.

Competing interests

The authors declare no competing interests.

Additional information

Supplementary information The online version contains supplementary material available at https://doi.org/10.1038/s41467-025-59748-5.

Correspondence and requests for materials should be addressed to Giuseppe Vecchi.

Peer review information *Nature Communications* thanks the anonymous reviewers for their contribution to the peer review of this work. A peer review file is available.